Near-Infrared Fluorescence Energy Transfer Imaging of Nanoparticle Accumulation and Dissociation Kinetics in Tumor-Bearing Mice

Yiming Zhao,[†,‡] Inge van Rooy,[‡,§] Sjoerd Hak,[⊥] Francois Fay,[‡] Jun Tang,[‡,∥] Catharina de Lange Davies,[#] Mihaela Skobe,[△] Edward Allen Fisher,[▽] Aurelian Radu,[§] Zahi. A. Fayad,[‡] Celso de Mello Donegá,[†] Andries Meijerink,[†] and Willem J. M. Mulder[‡,□,*]

[†]Condensed Matter and Interfaces, Debye Institute for Nanomaterials Science, Utrecht University, Princetonplein 5, 3584 CC Utrecht, The Netherlands, [‡]Translational and Molecular Imaging Institute, Icahn School of Medicine at Mount Sinai, One Gustave L. Levy Place, New York, New York 10029, United States, [§]Developmental and Regenerative Biology, Icahn School of Medicine at Mount Sinai, One Gustave L. Levy Place, New York, New York 10029, United States, [⊥]MI Lab and Department of Circulation and Medical Imaging, The Norwegian University of Science and Technology, Trondheim, Norway, [∥]Graduate School of Biological Sciences, Icahn School of Medicine at Mount Sinai, One Gustave L. Levy Place, New York, New York 10029, United States, [#]Department of Physics, The Norwegian University of Science and Technology, Trondheim, Norway, [△]Derald H. Ruttenberg Cancer Center, Icahn School of Medicine at Mount Sinai, One Gustave L. Levy Place, New York, New York 10029, United States, [▽]Langone Medical Center, New York University, New York, United States, and [□]Department of Vascular Medicine, Academic Medical Center, Amsterdam, The Netherlands

ABSTRACT In the current study we show the dissociation and tumor accumulation dynamics of dual-labeled near-infrared quantum dot core self-assembled lipidic nanoparticles (SALNPs) in a mouse model upon intravenous administration. Using advanced *in vivo* fluorescence energy transfer imaging techniques, we observed swift exchange with plasma protein components in the blood and progressive SALNP dissociation and subsequent trafficking of individual SALNP components following tumor accumulation. Our results suggest that upon intravenous administration SALNPs quickly transform, which may affect their functionality. The presented technology provides a modular *in vivo* tool to visualize SALNP behavior in real time and may contribute to improving the therapeutic outcome or molecular imaging signature of SALNPs.

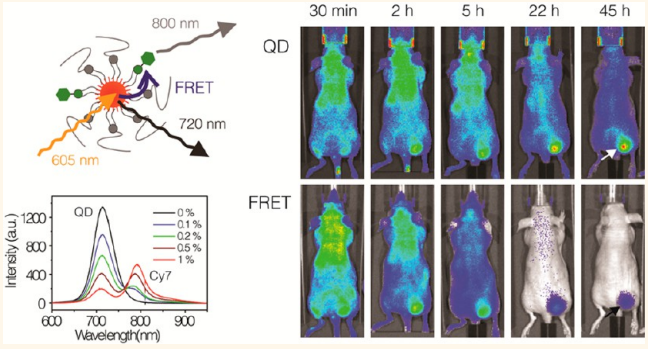

KEYWORDS: quantum dots · Förster resonance energy transfer · *in vivo* imaging · tumor-bearing mice · lipidic nanoparticles

In the last two decades self-assembled lipidic nanoparticles (SALNPs) have been shown to be broadly applicable as intravenously injectable agents for biomedical purposes.[1−5] SALNPs can serve as delivery vehicles for a wide variety of drugs, ranging from cytostatic agents to small interfering RNAs (siRNA) and proteins, and as molecular imaging probes.

Since their introduction by Dubertret and colleagues,[6] hybrid SALNPs that consist of a nanocrystal core covered by a self-assembled lipid coating have been widely explored as imaging agents, as many nanocrystals exhibit unique diagnostic features.[1,7] These hybrid SALNPs possess unprecedented possibilities with respect to their multifunctionality and potential for derivatization and biocompatibility, as well as to serve as drug targeting vehicles.[5,8]

The flexibility and versatility of SALNPs derive from their self-assembled nature, which allows facile inclusion and exchange of functional components as well as fine-tuning of composition. Despite their widespread application in *in vivo* studies, primarily for preclinical cancer diagnosis and therapy,[5,9] studies that address the dissociation kinetics of self-assembled nanoparticles, including SALNPs, after intravenous

* Address orrespondence to willem.mulder@mssm.edu.

Received for review September 12, 2013 and accepted October 17, 2013.

Published online October 17, 2013
10.1021/nn404782p

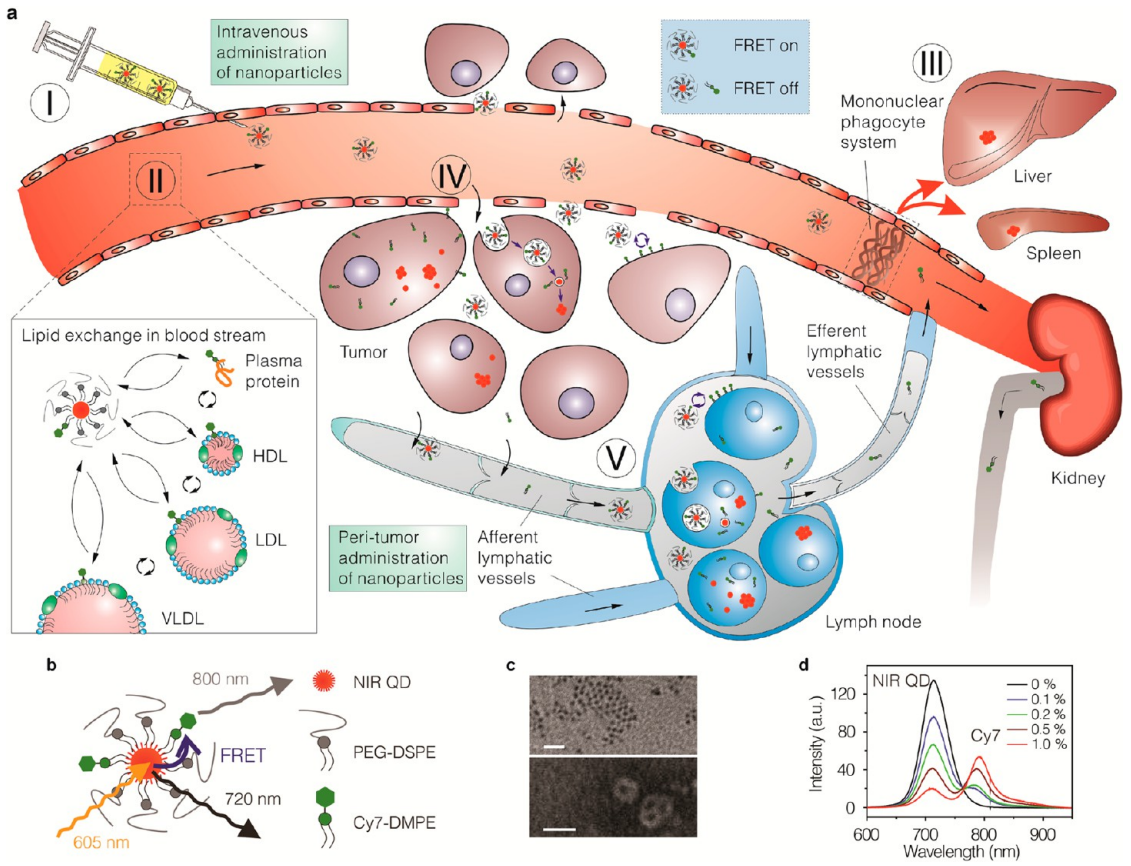

Figure 1. Schematic of nanoparticle trafficking and fate upon intravenous administration. (a) Schematic illustration of the blood circulation, dissociation dynamics, tumor accumulation, and trafficking of self-assembled nanoparticles upon intravenous administration (I) in a tumor-bearing mouse. Several distinct compartments include the blood (II), the tumor (IV, interstitium), lymphatics and lymph nodes (V), and clearance organs of the mononuclear phagocyte system (III). (b) Schematic structure of a self-assembled lipid nanoparticle that consists of a near-infrared quantum dot core covered by a self-assembled lipid coating that is composed of Cy7-labeled and PEGylated lipids (QD710-Cy7-PEG). (c) TEM images of QD710-Cy7-PEG with (lower) and without negative staining (upper). Both scale bars are 20 nm. (d) Emission spectra of QD710-Cy7-PEG nanoparticles in PBS with different percentages of Cy7-lipids in the lipid corona. λ_{Exc} = 500 nm. At increasing content of Cy7-lipids, the QD emission decreased dramatically, while Cy7 emission increased correspondingly, confirming the occurrence of FRET from the QD cores to the Cy7 dyes in the corona.

administration are scarce.[10] However, in order to maintain their functionality and fulfill their targeting purpose, the integrity of the assembled nanoparticle structure is crucial. Upon intravenous administration (Figure 1a, I), SALNPs are initially exposed to plasma proteins, lipoproteins, and circulating cells (Figure 1a, II).[10−12] In addition, they are exposed to the mononuclear phagocyte system (MPS), *i.e.*, splenic phagocytic cells and the Kupffer cells of the liver (Figure 1a, III).[13] After extravasation from the vasculature into, for example, the tumor interstitium (Figure 1a, IV), facilitated by the highly permeable tumor vasculature, nanoparticles may interact with components of the extracellular matrix, tumor-associated macrophages, and/or tumor cells.[14] Finally, upon their dissociation and draining into the lymphatic system, nanoparticles or nanoparticle components may be retained by lymphocytes (Figure 1a, V).[15,16]

In a previous study, we have successfully studied the dynamics of lipoprotein interactions *in vitro* using quantum dot (QD) and Cy5.5 dual-labeled nanoparticles using Förster resonance energy transfer (FRET) principles.[17] In the current study we further developed this technology to monitor these processes in real time by *in vivo* fluorescence imaging techniques. To that end we advanced the design of our dual-labeled nanoparticle by tuning its optical features to the near-infrared (NIR). In combination with various advanced florescence imaging technologies, this nanoparticle allowed us to investigate the dynamics of nanoparticle accumulation and dissociation in a tumor mouse model.

RESULTS AND DISCUSSION

Highly efficient and air-stable CdTe/CdSe/CdS/ZnS core/multishell QDs were synthesized to serve as a FRET donor. Their emission band was tuned to center at 710 nm (see Supporting Information, SI, Methods and TEM images in Figure S1). These QDs were coated by a PEGylated self-assembled lipid monolayer,[6] and the dye−lipids incorporated in this nanoparticle corona functioned as 800 nm emitting FRET acceptors.

The resulting nanoparticle (QD710-Cy7-PEG) is schematically presented in Figure 1b. Negative staining transmission electron microscopy (TEM) images confirmed a lipid corona covering a single QD nanocrystal (Figure 1c). The occurrence of FRET was confirmed by measuring emission spectra of a series of these particles containing varying amounts of Cy7-lipids. As plotted in Figure 1d, with increasing Cy7-lipid content, the QD emission at 710 nm decreased, while the dye emission at 800 nm increased correspondingly. We further measured the QD emission lifetime of these samples and observed a decrease in lifetime, which corroborated that the above intensity changes were due to FRET (SI Figure S3).[18,19]

The large spectral separation between the QD and Cy7-lipid enables us to trace the individual nanoparticle components simultaneously, while FRET between the QD core and the Cy7-lipid allows sensitive and semiquantitative monitoring of the dissociation of the lipid corona from the QD core. To test the possibility of studying this FRET principle in an *in vivo* pilot experiment, QD710-Cy7-PEG was subcutaneously injected into the dorsal side of nude mice. Similar to *in vitro* conditions,[17] dissociation of Cy7-lipids could be directly detected as an increase in QD intensity and simultaneous decrease of FRET intensity (SI Figure S4).

Subsequently, nude mice bearing HCT116 colon carcinoma on their flank were intravenously administered with either FRET QD710-Cy7-PEG or control QD710-PEG and subjected to NIR fluorescence imaging. FRET QD710-Cy7-PEG accumulation in the tumor was observed as early as 30 min postadministration (Figure 2a). Complete image data sets and control groups are included in SI Figures S5−8. Region of interest (ROI) analyses of the tumors revealed different dynamics for the different components (Figure 2b). For control QDs (QD710-PEG), the signal kept increasing for about 2 h and then slowly declined over 48 h. However, for the dual-labeled FRET QD710-Cy7-PEG, the QD signal increased much faster in the initial 2 h and kept rising even past 24 h. This initial faster increase was indicative of the disassociation of Cy7-lipids from the nanoparticle, which caused dequenching of QD emission. The subsequent gradual elevation of QD emission from the tumor by far exceeded the blood presence of the nanoparticles, which we established to have about a one-hour circulation half-life (SI Figure S9). Conversely, after an initial increase, the Cy7 signal started to decrease after 2 h and gradually vanished over 48 h. A similar pattern was observed for the FRET intensity (Figure 2a,b), which confirmed the Cy7-lipid dissociation from the nanoparticles after tumor accumulation.

Ex vivo NIR fluorescence imaging of organs revealed FRET QD710-Cy7-PEG to be accumulated in the tumor and major organs (liver, spleen, and kidneys). QD intensities were higher at 48 h than 8 h (Figure 2c,d), suggesting that the dequenching effect due to the dissociation of Cy7-lipid also occurred in these organs. As opposed to the QD intensities, Cy7 intensities in all the organs decreased from 8 h to 48 h (Figure 2e,f), which indicated that the Cy7-lipid had a clearly different biodistribution compared to QDs. The presence of Cy7-lipids in the kidneys suggests trafficking of this component to the kidneys and subsequent renal clearance. Fluorescence microscopy (FM) of tumor and liver tissues revealed the QDs to be mainly present as clusters, while the Cy7-lipids were found diffusely throughout the cytoplasm (Figure 2g and SI Figures S10, S11). TEM images confirmed the presence of dense QD aggregates and additionally demonstrated that the QDs had entered cells and were mainly localized inside vesicles of tumor and liver cells (Figure 2h). Altogether, the *ex vivo* microscopy data corroborated the dissociation of the coating lipids from the QDs.

Tumors grown in dorsal window chambers (SI Figure S12) allowed us to study the dissociation and nanoparticle kinetics in the tumor blood vessels and in the tumor interstitium with intravital confocal laser scanning microscopy (CLSM).[14,20] To that end 610 nm emitting QD610 and Cy5.5-lipid labeled nanoparticles (QD610-Cy5.5-PEG) were employed (see emission spectra in SI Figure S13). Extravasation of QDs and Cy5.5-lipids from the vasculature into the tumor interstitium was clearly observed within 2 h postadministration (Figure 3a, SI Movies S1−3). ROI analyses of the vascular and extravascular space revealed different dynamics for the QDs and Cy5.5-lipids in both these compartments (Figures 3b−d). In blood vessels the Cy5.5 and FRET signal decreased more rapidly than the QD signal, indicative of nanoparticle dissociation in circulation (Figure 3b and SI Figure S14). Conversely, extravascularly the QD signal kept increasing in the first 2 h, while the Cy5.5 and FRET intensities started to decrease after 1 h. This behavior is similar to what we observed with whole body NIR imaging (Figure 2b). In Figure 3d, an overall decrease of FRET/QD ratio confirmed the dissociation of Cy5.5-lipids from the lipid-coated QDs within the first 2 h after administration, in both the vascular and extravascular space. The lipid dissociation constant was derived from fitting the vascular FRET/QD ratio with a monoexponential decay function.[21] We found this constant to be $2.7 \times 10^{-4}\ s^{-1}$ and the dissociation half-life to be around 42 min, indicating that the majority of the Cy5.5-lipids were dissociated from the QD after the first 2 h. At 48 h a distinct dissociation of QD cores and Cy5.5-lipids was observed in the tumor interstitium (Figure 3a and SI Figure S15).

The interaction between nanoparticles and serum proteins has recently been investigated by us and others.[10,11,17,22] The afore-presented results indicated that the lipid-coated nanocrystals also vividly exchange coating lipids with blood proteins. Fast protein liquid

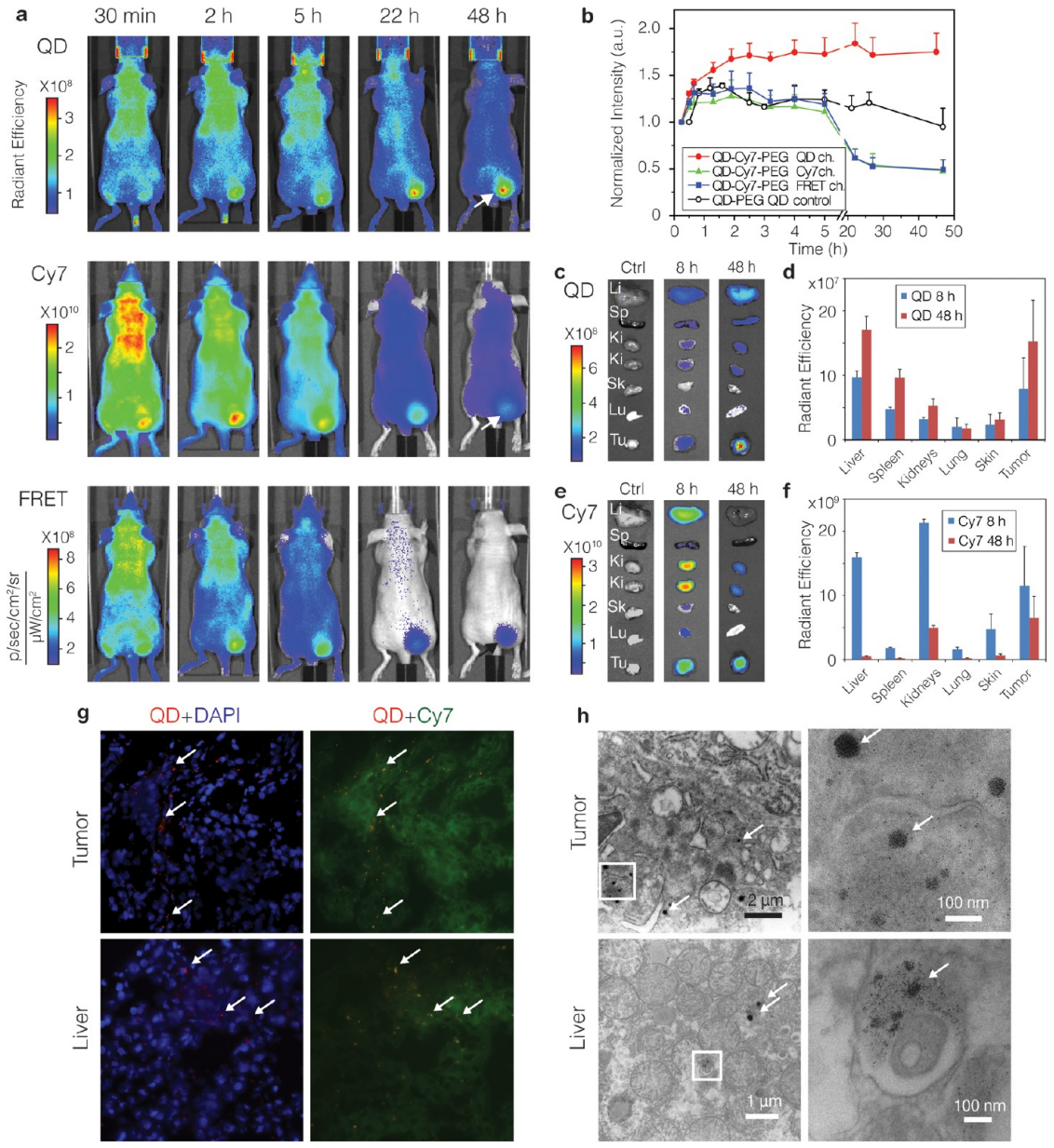

Figure 2. Accumulation and dissociation of QD710-Cy7-PEG in xenograft tumor mouse model upon intravenous administration. (a) Representative *in vivo* NIR fluorescence images of a tumor-bearing mouse injected with 100 pmol/g FRET particles QD710-Cy7-PEG at 30 min and 2, 5, 22, and 48 h postinjection. Tumor mice injected with 100 pmol/g QD710-PEG nanoparticles containing no Cy7-lipids were used as QD control. Fluorescent signal was collected using three optical filters settings: QD (λ_{Exc} = 605 ± 18 nm, λ_{Em} = 720 ± 10 nm), Cy7 (λ_{Exc} =745 ± 18 nm, λ_{Em} = 800 ± 10 nm), and FRET (λ_{Exc} = 605 ± 18 nm, λ_{Em} = 800 ± 10 nm). (b) The mean intensities (n = 5 mice per group) from the tumor area (indicatad with arrows in a) plotted against postinjection time. QD, Cy7, and FRET intensities were from mice injected with QD710-Cy7-PEG, and QD control was from mice injected with QD710-PEG. Mice were sacrificed at 8 h (n = 3) and 48 h (n = 5) after injection, and major organs were subjected to *ex vivo* fluorescence imaging. Representative images and mean intensities from the organs are presented in c and d for the QD channel and in e and f for the Cy7 channel. Li, liver; Sp, spleen; Ki, kidney; Sk, skin; Lu, lung; Tu, tumor. (g) Fluorescence microscopy images of frozen sections of tumor (upper row) and liver (lower row) tissue sections at 48 h postinjection. Signal from QD (λ_{Exc} = 620 ± 30 nm, λ_{Em} = 700 ± 35 nm) is red, DAPI for nucleus staining (λ_{Exc} = 350 ± 30 nm, λ_{Em}= 460 ± 22 nm) is blue, and Cy7 (λ_{Exc} = 710 ± 35 nm, λ_{Em} = 810 ± 40 nm) is green. Aggregates of QD cores are indicated by arrows. (h) Stained transmission electron microscopy (TEM) images of tumor (upper row) and liver (lower row) tissues at 48 h after injection. Insets are magnified on the right. Aggregates of QD cores are indicated by arrows.

chromatography (FPLC)[23] was employed to study different plasma fractions collected at 2, 8, and 48 h after intravenous administration of QD610-Cy5.5-PEG. At 2 h postinjection, the dominant QDs and Cy5.5-lipid intensities were found in different fractions (Figure 3e), indicating that the nanoparticle remaining in blood had already dissociated with their lipid coating through lipid exchange while in circulation, which is consistent with the dissociation rate determined above. Although at early time points the majority of Cy5.5-lipids were found associated with small plasma proteins (<5 nm), at 48 h the main Cy5.5 intensity was observed in the

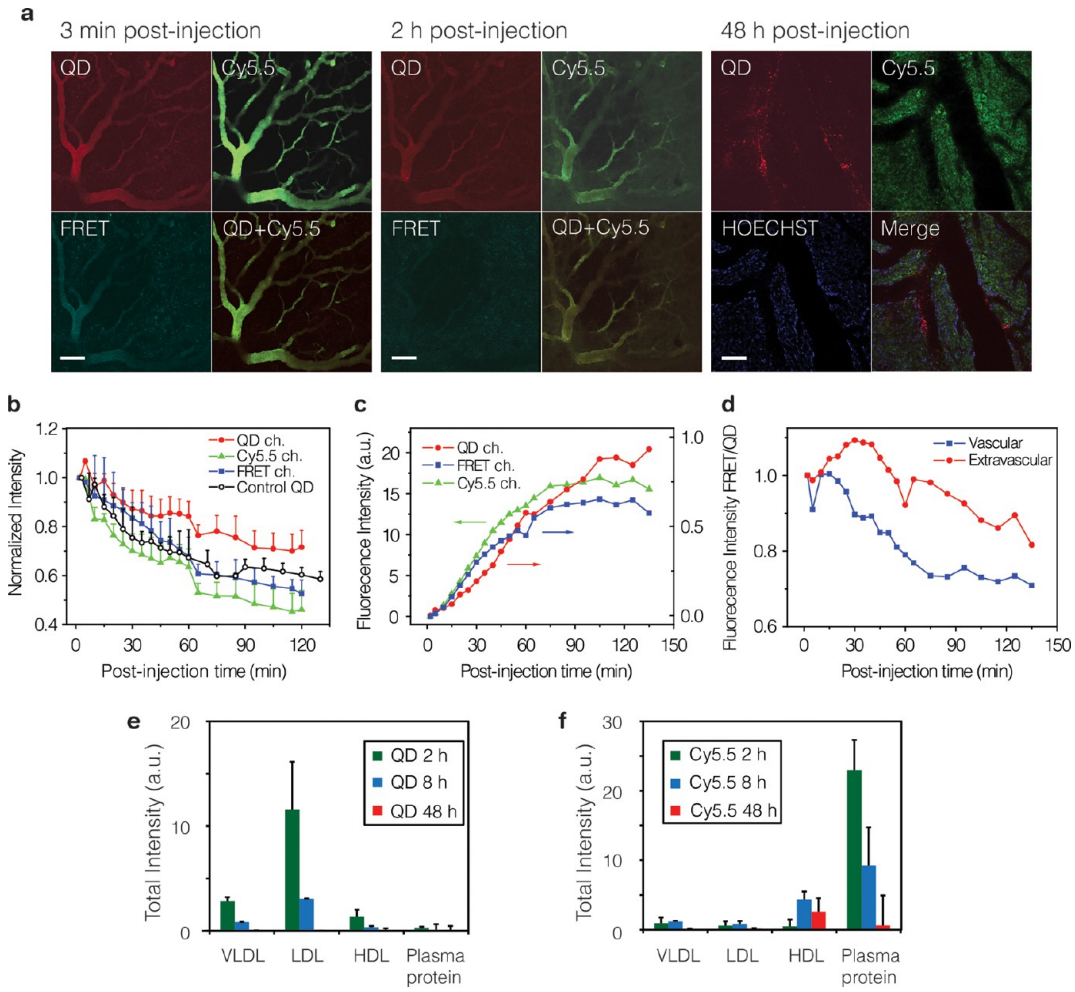

Figure 3. Intravital microscopy of tumors grown in a window chamber and FPLC investigation of the dynamics of lipid-coated nanocrystal. (a) Mice with tumor grown in a window chamber were injected with 130 pmol/g QD610-Cy5.5-PEG, continuously observed for 2 h, and discretely observed until 48 h postadministration. Representative fluorescence images at 30 min, 2 h, and 48 h are shown in a. The scale bar represents 100 μm. Four optical channels were used: QD (λ_{Exc} = 488 nm, λ_{Em} = 612−655 nm) is shown in red, Cy5.5 (λ_{Exc} = 633 nm, λ_{Em} = 698−719 nm) is shown in green, FRET (λ_{Exc} = 488 nm, λ_{Em} = 698−719 nm) is shown in cyan, and HOECHST for nucleus staining (λ_{Exc} = 780 nm, λ_{Em} = 435−485 nm) is shown in blue. The normalized fluorescence intensities in three channels (QD in filled circles, Cy5.5 in filled triangles and FRET in filled square) are plotted against postinjection time for the vascular in b and for extravascular space in c. QD610-PEG nanoparticles containing non-Cy5.5-lipids were used as QD control (empty circles). (d) The FRET/QD intensity ratios derived from the graphs in b and c represent the relative extent of FRET per QD and are plotted against time. Plasma collected from mice at 2, 8, and 48 h after injection with 100 pm/g QD-Cy5.5-PEG (n = 3 animals for each time point) separated in different fractions using fast protein liquid chromatography (FPLC). The total fluorescent intensities from four different protein fractions, VLDL (25−90 nm), LDL (18−25 nm), HDL (5−15 nm), and small plasma proteins (<5 nm), are summarized (e) for QD signal (λ_{Exc} = 430 ± 18 nm, λ_{Em}= 620 ± 10 nm) and (f) for Cy5.5 signal (λ_{Exc} = 640 ± 18 nm, λ_{Em} = 700 ± 10 nm).

HDL fraction (5−10 nm). This observation was in agreement with the clearance data for the Cy7/Cy5.5-labeled lipids, where Cy5.5-lipids associated with small plasma proteins could be cleared renally, while labeled lipids that were associated with HDL could be retained as a result of the renal clearance threshold of around 5.5 nm.[24,25] The latter caused Cy5.5-lipids to be mainly present in the HDL fractions at later time points.

To better understand lymphatic drainage dynamics of the nanoparticles in the sentinel lymph node (SLN), we isolated this process by injecting QD710-Cy7-PEG in the periphery of solid tumors in nude mice.[15,16] A representative NIR fluorescence image of this process is presented in Figure 4a. We observed the nanoparticles drained from the tumor and migrated to the inguinal lymph nodes (as SLN) within minutes. ROI analyses on the SLN revealed different dynamics for QDs and Cy7-lipids (Figure 4b), suggesting that after the nanoparticles reached the SLN the QD cores were retained and Cy7-lipids were moved away. *Ex vivo* fluorescence imaging of SLN and organs was performed at 5 and 45 h postadministration to mimic a situation where nanoparticles are first allowed to accumulate in the tumor for 3 h after intravenous administration. Here, we also observed a difference in biodistribution between QDs and Cy7-lipids. The QDs were mostly retained in the SLN, and their intensity increased from 5 h to 45 h, due to dissociation of Cy7-lipids (Figure 4c,d).

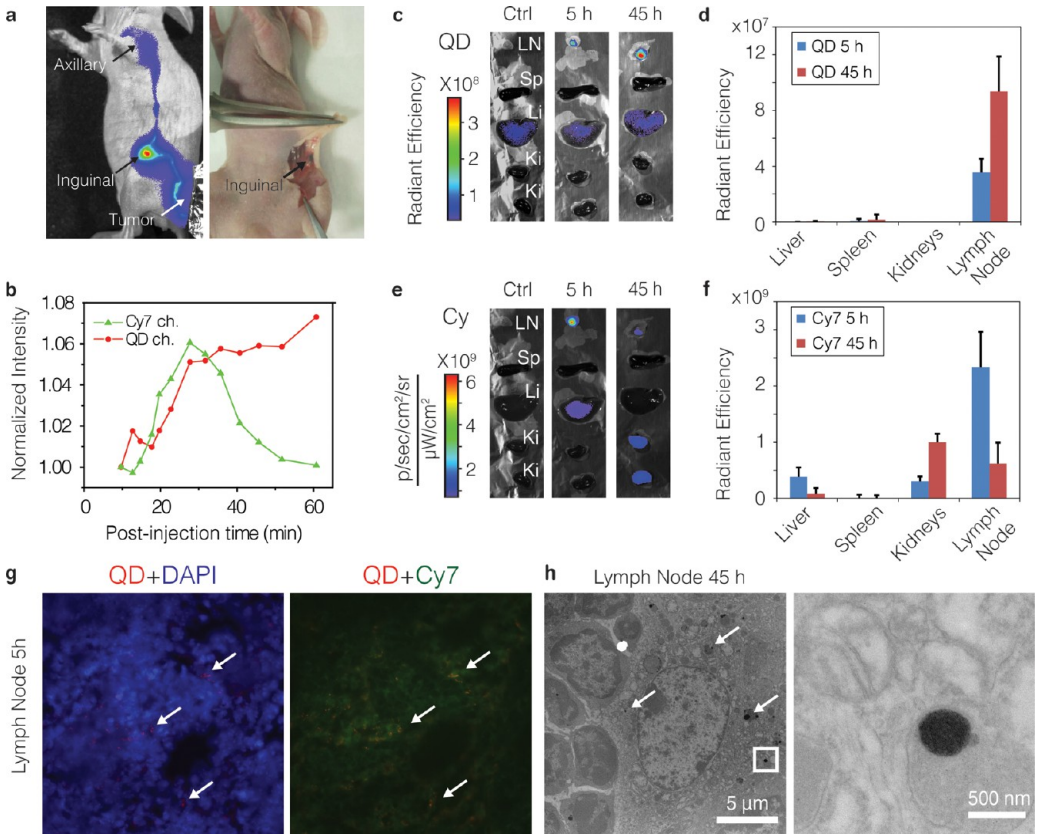

Figure 4. Peri-tumoral administration of lipid-coated nanocrystals. (a) NIR fluorescence image (left, laid over bright field image) showing in both the QD and the Cy7 channel (Cy7 channel shown here) that the QD710-Cy7-PEG migrated through lymphatic drainage from the periphery of the tumor to the inguinal node (as a sentinel lymph node (SLN)) and further to the axillary node. After reinjection with 1% Evans blue, QD710-Cy7-PEG and Evans blue were found co-localized in the same lymph node, as indicated by the arrows (a, right, color image). (b) Normalized total fluorescent intensities of QD710 (squares) and Cy7 (triangles) from the SLNs are plotted against postinjection time, showing their different dynamic behaviors. Mice were sacrificed at 5 and 45 h postinjection ($n = 3$ for each time point). Subsequently, the inguinal node and major organs were subject to *ex vivo* fluorescence imaging. Representative images and mean intensities are depicted in c and d for the QD channel and in e and f for the Cy7 channel. LN, lymph node. (g) Fluorescence microscopy images of SLN tissue at 5 h postinjection. Merged images are shown with the signal from QD (red), Cy7 (green), and DAPI (blue). Spots of QD accumulations are indicated with arrows. (h) TEM images of SLN tissues at 45 h after injection. Aggregates of QD cores inside the phagocyte are indicated by arrows. Inset is enhanced on the right.

Conversely, the intensity of the Cy7-lipid in the SLN decreased over time, and its presence in the liver and kidneys was observed (Figure 4 e,f), implying trafficking of this component to these organs and subsequent renal clearance (Figure 1a). FM (Figure 4g) and TEM images (Figure 4h) of excised SLNs revealed the QDs to be aggregated inside phagocytes and not to be co-localized with the Cy7-lipids.

In summary, SALNPs are dynamic structures that progressively disintegrate due to a lipid exchange process after intravenous administration (Figure 1a, I, II). Upon vascular extravasation and accumulation in the tumor interstitium, this process continues (Figure 1a, IV). In the case of the QD core SALNPs used in the current study, cellular internalization causes the QD cores to sequester in the tumor, lymph nodes, and MPS organs (Figure 1a, III, V), while their coating lipids partially follow different clearance kinetics in the circulatory system and can also be cleared renally.

Although the *in vivo* dissociation behavior and the nanoparticle stability found in the current study are valid only for the particular type of SALNPs studied,[1,6] the multifaceted strategy we developed to assess the *in vivo* stability by FRET is flexible and applicable to a wide variety of SALNPs, including lipid–polymer hybrid nanoparticles[26] and lipoprotein-derived nanoparticles,[27] Moreover, it can be used to evaluate differently formulated SALNPs and screen for compositions with improved stability.[17]

CONCLUSION

Our approach represents a modular *in vivo* optical imaging tool to visualize the behavior of self-assembled nanoparticles in real time and may contribute to enhancing the therapeutic outcome or improving the molecular imaging signature of this widely used class of nanoparticles. The *in vivo* dissociation behavior of SALNPs may influence their drug delivery efficiency and may also have implications for other

types of self-assembled nanoparticles, such as nanoparticles comprised of block copolymers.[28,29] Our study also provides a framework to improve the specificity of self-assembled diagnostic nanoparticles since the *in vivo* integrity of such systems can now be carefully monitored. At the same time the exchange phenomenon may be exploited to transfer amphiphilic agents, such as cholesterol-derivitized siRNAs[30] or diagnostically active amphiphiles,[1] from SALNPs to lipoproteins in the body.

METHODS

Synthesis of Cy7-DMPE-Labeled PEG-DSPE-Coated NIR Quantum Dot Micelles (QD710-Cy7-PEG). Synthesis of the NIR QD is described in the SI methods. For the synthesis of QD710-Cy7-PEG, a typical process is described below. A 20 μmol amount of DSPE-PEG2000 and 1 nmol of NIR-QDs were dispersed in 0.5 mL of chloroform. Cy7-labeled lipid was added to this mixture at various molar percentages of 0%, 0.1%, 0.2%, 0.5%, and 1%. The dispersion was dripped into 2 mL of heated (over 80 °C) deionized water under vigorous stirring. After all the organic solvent was evaporated, this water dispersion was centrifuged at 2000 rpm for 10 min to remove uncoated QDs and large aggregates. The QD micelle dispersion was then purified by centrifuging 200 μL on top of 1 mL of 30% w/w KBr solution at 14 500 rpm for 2 h using a microcentrifuge tube. Centrifugation transferred the QD micelles into the KBr layer, and the top 250 μL containing empty micelles and free lipids was taken off and discarded. The remaining solution was collected (precipitation on the bottom of tube was discarded) and washed/desalted three times with PBS using a Vivaspin 30 000 MWCO tube. The nanoparticle solution was finally enriched to the desired concentration by Vivaspin centrifugation.

Cell Culture and Tumor Model. HCT-116 cells were obtained from the Tumor Cell Biorepository of the Department of Oncological Sciences at the Icahn School of Medicine at Mount Sinai and were cultured at 37 °C under 5% CO_2 in DMEM culture medium, supplemented with 10% FBS.

Six-week-old female Swiss nude mice were obtained from Taconic (Albany, NY, USA) and were supplied with water and a standard rodent chow *ad libitum*. Five days before NIR fluorescent imaging, the diet was changed to AIN-93 M maintenance purified diet (TestDiet, Richmond, IN, USA) in order to reduce the autofluorescent background. All animal handling was approved by the Icahn School of Medicine at Mount Sinai Institutional Animal Care and Use Committee. The tumor model was established by inoculation of 2.5 million HCT-116 cells, suspended in 50 μL of serum-free DMEM, on the right side flank of the mice. Tumors were grown for 2 weeks to an average volume of 400 mm^3, as measured with a digital caliper and by applying the formula $V = 0.52 \times a^2 \times b$, where a is the smallest measured diameter and b is the largest measured diameter.

***In Vivo* Fluorescence Imaging.** Tumor-bearing mice were injected intravenously by tail vein with QD710-Cy7-PEG or QD710-PEG at a dose of 100 pmol/g ($n = 5$). For each experimental group, NIR fluorescence images of the mice were recorded at various time points after injection (t = 0.25, 0.5, 0.66, 1.3, 1.9, 2.5, 3.2, 4, 5, 22, 27, 45 h) using a Xenogen IVIS Spectrum imaging system (Alemeda, CA, USA). Mice were anesthetized using vaporized isoflurane, with a 4% induction dose, and five mice at a time were positioned in the IVIS with isoflurane administered at 1.5% *via* a nose cone. Three optical channels were recorded with selected excitation and emission band-pass filters: QD ($\lambda_{Exc} = 605 \pm 18$ nm, $\lambda_{Em} = 720 \pm 10$ nm), Cy7 ($\lambda_{Exc} = 745 \pm 18$ nm, $\lambda_{Em} = 800 \pm 10$ nm), and FRET ($\lambda_{Exc} = 605 \pm 18$ nm, $\lambda_{Em} = 800 \pm 10$ nm). Overall acquisition time was 20 s, and all settings were kept the same for each time point, enabling comparison of intensity values. Results were processed and analyzed using Living Image software by drawing a region of interest in the tumor area.

***Ex Vivo* Organ Fluorescence Imaging.** The mice that were administered QD710-Cy7-PEG nanoparticles intravenously were sacrificed after 8 h ($n = 3$) or 48 h ($n = 5$) postinjection and were perfused through the heart with 40 mL of PBS. Tumors and major organs were harvested and subject to fluorescent imaging immediately in the three optical channels described above. Organs from uninjected mice were used as blank control.

TEM of Tumor, Lymph Node, and Other Tissues. The tumor, lymph node, liver, spleen, and kidney from the above-mentioned sacrificed mice were cut into small pieces and fixed in 2.5% glutaraldehyde. The tissue samples were processed by a standard procedure with osmium tetraoxide and embedded in epoxy resin blocks. The resin blocks were cut into 60 nm sections with a microtome and placed on TEM grids. The sample grids were poststained with 4% uranyl acetate and lead citrate before imaging. The TEM imaging used the same electron microscopy and conditions as previously described for nanoparticle characterization.

Fluorescence Microscopy. Tissue samples of tumor, lymph node, liver, spleen, and kidney from the above-mentioned sacrificed mice were embedded in OCT embedding matrix and frozen at −20 °C. Sections of 5 μm were cut on a cryostat and transferred to glass microscope slides. Upon use, sections were thawed for 20 min and mounted in Vectashield mounting medium with DAPI (Vector Laboratories, Burlingame, CA, USA). Sections were imaged using a Zeiss Axioplan 2 widefield microscope (Zeiss, Jena, Germany) equipped with Cy5 and Cy7 filters (Chroma 49000 series, Chroma Technology Corp, Bellows Falls, VT, USA) for imaging of QD710 and Cy7 dye, respectively. Cy5 exposure times were 100, 500, and 1500 ms for liver, lymph node, and tumor, respectively. Cy7 exposure times were 2000 ms for liver and 4000 ms for lymph node and tumor tissues. Cy5 and Cy7 exposure times were kept constant per tissue for QD710-Cy7 and QD710 samples. Magnification was 40 times in all fluorescence microscopy images.

Intravital Microscopy. For intravital confocal laser scanning microscopy (Zeiss LSM 510 META), tumors grown in dorsal window chambers in mice were used. The mice were anesthetized with a subcutaneous injection of 12 mg/kg midazolam/fentanyl/haloperidol/water (3/3/2/4), and the window chambers (made of polyoxymethylene, built in-house) were implanted as previously described in male athymic Balb/c Nu/nu mice of 22 to 24 g.[31] Twenty-four hours after implanting the chambers, $(2-3) \times 10^6$ HCT-116 cells were injected in the center of each chamber. The surgical procedures were performed under sterile conditions. The animals were kept under pathogen-free conditions at a temperature of 19 to 22 °C, 50% to 60% humidity, and 65 air changes per hour, and animals were allowed food and water (which contained 2% sucrose and 67.5 mg/L Baytril (enrofloxacin)) *ad libitum*. Sixteen to 18 days after implantation, when the tumors were 0.2 to 0.3 cm thick and filled 30−60% of the window area, the mice were used for experiments.

The mice were anesthetized by subcutaneous injections of 12 mg/kg midazolam/fentanyl/Haldol/water (3/3/2/4), got a catheter (BD Venflon) placed in the tail vein, and were placed on a custom-built temperature-controlled CLSM imaging stage. The tumors were imaged using a long working distance Plan-Neofluor 20×/0.5 objective. DIC contrast was used to focus on tumor vasculature before injection, and subsequently either QD610-PEG ($n = 2$) (but only one intravascular curve from only one mouse) or QD610-Cy5.5-PEG ($n = 2$) (but extravascular curve from only one) was injected at a dose of 130 pmol/g.

To study nanoparticle and lipid dissociation dynamics, the same tumor region was imaged repeatedly at 3, 5, 10, 15, 20, 25, 30, 35, 40, 45, 50, 55, 60, 70, 80, 90, 100, 110, 120 min postinjection. Subsequently, images were obtained throughout the tumor at several time points up to 48 h postinjection. HOECHST 33342 (Sigma) was injected 24 h postinjection of

the nanoparticles to visualize cell nuclei, facilitating the assessment of nanoparticle integrity and localization. QDs were excited at 488 nm and detected with the META system at 612−655 nm, and Cy5.5 was excited at 633 nm and detected with the META system at 698−719 nm. FRET was detected using 488 nm excitation and recording with the META system at 698−719 nm. HOECHST 33342 was excited using two-photon excitation at 780 nm and detected with a bandpass filter at 435−485 nm.

Images were analyzed with ImageJ software. The images obtained in the first 2 h postinjection were aligned and combined into one dynamic series. ROIs were drawn manually in the vasculature and extravascular space from which the fluorescence intensity *vs* time curves were obtained. Fluorescence intensities were normalized to the fluorescence intensity observed 3 min postinjection. The FRET/QD ratio was obtained by dividing the normalized fluorescence intensities.

Fast Protein Liquid Chromatography. Tumor-bearing nude mice ($n = 9$) were anesthetized using isoflurane, and for each mouse 100 pmol/g QD610-Cy5.5-PEG was administrated intravenously by tail vein injection. At 2, 8, and 48 h postinjection, three mice per time point were sacrificed, and 500 μL of blood was drawn from the left ventricle of the heart. Serum was obtained through centrifugation at 10k rpm for 2 $\times$ 10 min. Two Superose-6 FPLC columns in series (Shimazu LC solution) were pre-equilibrated with degassed filtrated buffer (0.15 M NaCl, 1 mM EDTA). Mouse serum samples were filtrated with a 0.22 μm pore size membrane, and 200 μL for each sample was injected to the columns. Samples were then eluted with equilibration buffer while the absorbance of eluted solution was monitored at 280 nm. The eluent was collected and divided into four effective fractions according to a predetermined retention time, which corresponded to the size of proteins: VLDL (25−90 nm), LDL (18−25 nm), HDL (5−15 nm), and small plasma proteins (<5 nm).[23] The fluorescence intensities of sample fractions were determined and analyzed by an IVIS imaging system. The QD signal in the different fractions was measured with $\lambda_{Exc} = 430 \pm 18$ nm, $\lambda_{Em} = 620 \pm 10$ nm, and the Cy5.5 signal was measured with $\lambda_{Exc} = 640 \pm 18$ nm and $\lambda_{Em} = 700 \pm 10$ nm.

Conflict of Interest: The authors declare no competing financial interest.

Acknowledgment. This work was financially supported by the division of Chemical Sciences (CW) of the Dutch Science Foundation (NWO) under grant number ECHO.06.B.047 (A.M.) and the National Heart, Lung, and Blood Institute, National Institutes of Health, as a Program of Excellence in Nanotechnology (PEN) Award, Contract #HHSN268201000045C, the NIH grants R01EB009638 (Z.A.F.), R01CA155432 (W.J.M.M.), and R21CA159075 (A.R.), and the Norwegian Cancer Society. We thank Yu Zhou for his help with fluorescence imaging and K. Sæterbø for implanting the dorsal window chambers in mice and culturing cells.

Supporting Information Available: Supporting methods, figures, and movies. This material is available free of charge *via* the Internet at http://pubs.acs.org.

REFERENCES AND NOTES

1. Mulder, W. J. M.; Strijkers, G. J.; van Tilborg, G. A. F.; Cormode, D. P.; Fayad, Z. A.; Nicolay, K. Nanoparticulate Assemblies of Amphiphiles and Diagnostically Active Materials for Multimodality Imaging. *Acc. Chem. Res.* **2009**, *42*, 904–914.
2. Shi, J.; Xiao, Z.; Kamaly, N.; Farokhzad, O. C. Self-Assembled Targeted Nanoparticles: Evolution of Technologies and Bench to Bedside Translation. *Acc. Chem. Res.* **2011**, *44*, 1123–1134.
3. Yoo, J. W.; Irvine, D. J.; Discher, D. E.; Mitragotri, S. Bio-Inspired, Bioengineered and Biomimetic Drug Delivery Carriers. *Nat. Rev. Drug Discovery* **2011**, *10*, 521–535.
4. Whitehead, K. A.; Langer, R.; Anderson, D. G. Knocking Down Barriers: Advances in siRNA Delivery. *Nat. Rev. Drug Discovery* **2009**, *8*, 129–38.
5. Peer, D.; Karp, J. M.; Hong, S.; Farokhzad, O. C.; Margalit, R.; Langer, R. Nanocarriers as an Emerging Platform for Cancer Therapy. *Nat. Nanotechnol.* **2007**, *2*, 751–760.
6. Dubertret, B.; Skourides, P.; Norris, D. J.; Noireaux, V.; Brivanlou, A. H.; Libchaber, A. *In Vivo* Imaging of Quantum Dots Encapsulated in Phospholipid Micelles. *Science* **2002**, *298*, 1759–1762.
7. Cormode, D. P.; Sanchez-Gaytan, B. L.; Mieszawska, A. J.; Fayad, Z. A.; Mulder, W. J. M. Inorganic Nanocrystals as Contrast Agents in MRI: Synthesis, Coating and Introduction of Multifunctionality. *NMR Biomed.* **2013**, *26*, 766–780.
8. Lobatto, M. E.; Fuster, V.; Fayad, Z. A.; Mulder, W. J. Perspectives and Opportunities for Nanomedicine in the Management of Atherosclerosis. *Nat. Rev. Drug Discovery* **2011**, *10*, 835–852.
9. Jain, R. K.; Stylianopoulos, T. Delivering Nanomedicine to Solid Tumors. *Nat. Rev. Clin. Oncol.* **2010**, *7*, 653–664.
10. Li, Y.; Budamagunta, M. S.; Luo, J.; Xiao, W.; Voss, J. C.; Lam, K. S. Probing of the Assembly Structure and Dynamics within Nanoparticles during Interaction with Blood Proteins. *ACS Nano* **2012**, *6*, 9485–9495.
11. Nel, A. E.; Madler, L.; Velegol, D.; Xia, T.; Hoek, E. M.; Somasundaran, P.; Klaessig, F.; Castranova, V.; Thompson, M. Understanding Biophysicochemical Interactions at the Nano-bio Interface. *Nat. Mater.* **2009**, *8*, 543–557.
12. Owens, D. E., 3rd; Peppas, N. A. Opsonization, Biodistribution, and Pharmacokinetics of Polymeric Nanoparticles. *Int. J. Pharm.* **2006**, *307*, 93–102.
13. Cormode, D. P.; Skajaa, G. O.; Delshad, A.; Parker, N.; Jarzyna, P. A.; Calcagno, C. G.; Merav, W.; Skajaa, T.; Briley-Saebo, K. C.; Bell, H. M.; *et al*. A Versatile and Tunable Coating Strategy Allows Control of Nanocrystal Delivery to Cell Types in the Liver. *Bioconjugate Chem.* **2011**, *22*, 353–361.
14. Hak, S.; Helgesen, E.; Hektoen, H. H.; Huuse, E. M.; Jarzyna, P. A.; Mulder, W. J. M.; Haraldseth, O.; Davies, C. D. L. The Effect of Nanoparticle Polyethylene Glycol Surface Density on Ligand-Directed Tumor Targeting Studied *in Vivo* by Dual Modality Imaging. *ACS Nano* **2012**, *6*, 5648–5658.
15. Ballou, B.; Ernst, L. A.; Andreko, S.; Harper, T.; Fitzpatrick, J. A.; Waggoner, A. S.; Bruchez, M. P. Sentinel Lymph Node Imaging Using Quantum Dots in Mouse Tumor Models. *Bioconjugate Chem.* **2007**, *18*, 389–396.
16. Kim, S.; Lim, Y. T.; Soltesz, E. G.; De Grand, A. M.; Lee, J.; Nakayama, A.; Parker, J. A.; Mihaljevic, T.; Laurence, R. G.; Dor, D. M.; *et al*. Near-Infrared Fluorescent Type II Quantum Dots for Sentinel Lymph Node Mapping. *Nat. Biotechnol.* **2004**, *22*, 93–97.
17. Skajaa, T.; Zhao, Y.; van den Heuvel, D. J.; Gerritsen, H. C.; Cormode, D. P.; Koole, R.; Parker, J. A.; Mihaljevic, T.; Laurence, R. G.; Dor, D. M. Quantum Dot and Cy5.5 Labeled Nanoparticles to Investigate Lipoprotein Biointeractions *via* Förster Resonance Energy Transfer. *Nano Lett.* **2010**, *10*, 5131–5138.
18. Medintz, I. L.; Clapp, A. R.; Mattoussi, H.; Goldman, E. R.; Fisher, B.; Mauro, J. M. Self-Assembled Nanoscale Biosensors Based on Quantum Dot FRET Donors. *Nat. Mater.* **2003**, *2*, 630–638.
19. Medintz, I. L.; Mattoussi, H. Quantum Dot-Based Resonance Energy Transfer and Its Growing Application in Biology. *Phys. Chem. Chem. Phys.* **2009**, *11*, 17–45.
20. Hak, S.; Reitan, N. K.; Haraldseth, O.; de Lange Davies, C. Intravital Microscopy in Window Chambers: A Unique Tool to Study Tumor Angiogenesis and Delivery of Nanoparticles. *Angiogenesis* **2010**, *13*, 113–130.
21. Reulen, S. W.; Merkx, M. Exchange Kinetics of Protein-Functionalized Micelles and Liposomes Studied by Forster Resonance Energy Transfer. *Bioconjugate Chem.* **2010**, *21*, 860–866.
22. Salvati, A.; Pitek, A. S.; Monopoli, M. P.; Prapainop, K.; Bombelli, F. B.; Hristov, D. R.; Kelly, P. M.; Aberg, C.; Mahon, E.; Dawson, K. A. Transferrin-Functionalized Nanoparticles Lose Their Targeting Capabilities When a Biomolecule Corona Adsorbs on the Surface. *Nat. Nanotechnol.* **2013**, *8*, 137–143.

23. Frias, J. C.; Ma, Y.; Williams, K. J.; Fayad, Z. A.; Fisher, E. A. Properties of a Versatile Nanoparticle Platform Contrast Agent To Image and Characterize Atherosclerotic Plaques by Magnetic Resonance Imaging. *Nano Lett.* **2006**, *6*, 2220–2224.
24. Choi, H. S.; Liu, W.; Misra, P.; Tanaka, E.; Zimmer, J. P.; Itty Ipe, B.; Bawendi, M. G.; Frangioni, J. V. Renal Clearance of Quantum Dots. *Nat. Biotechnol.* **2007**, *25*, 1165–1170.
25. Choi, H. S.; Liu, W.; Liu, F.; Nasr, K.; Misra, P.; Bawendi, M. G.; Frangioni, J. V. Design Considerations for Tumour-Targeted Nanoparticles. *Nat. Nanotechnol.* **2010**, *5*, 42–47.
26. Valencia, P. M.; Basto, P. A.; Zhang, L.; Rhee, M.; Langer, R.; Farokhzad, O. C.; Karnik, R. Single-Step Assembly of Homogenous Lipid−Polymeric and Lipid−Quantum Dot Nanoparticles Enabled by Microfluidic Rapid Mixing. *ACS Nano* **2010**, *4*, 1671–1679.
27. Bruns, O. T.; Ittrich, H.; Peldschus, K.; Kaul, M. G.; Tromsdorf, U. I.; Lauterwasser, J.; Nikolic, M. S.; Mollwitz, B.; Merkel, M.; Bigall, N. C.; *et al*. Real-Time Magnetic Resonance Imaging and Quantification of Lipoprotein Metabolism *in Vivo* Using Nanocrystals. *Nat. Nanotechnol.* **2009**, *4*, 193–201.
28. Euliss, L. E.; Grancharov, S. G.; O'Brien, S.; Deming, T. J.; Stucky, G. D.; Murray, C. B.; Held, G. A. Cooperative Assembly of Magnetic Nanoparticles and Block Copolypeptides in Aqueous Media. *Nano Lett.* **2003**, *3*, 1489–1493.
29. Berret, J.-F.; Schonbeck, N.; Gazeau, F.; El Kharrat, D.; Sandre, O.; Vacher, A.; Airiau, M. Controlled Clustering of Superparamagnetic Nanoparticles Using Block Copolymers: Design of New Contrast Agents for Magnetic Resonance Imaging. *J. Am. Chem. Soc.* **2006**, *128*, 1755–1761.
30. Schroeder, A.; Levins, C. G.; Cortez, C.; Langer, R.; Anderson, D. G. Lipid-Based Nanotherapeutics for siRNA Delivery. *J. Intern. Med.* **2010**, *267*, 9–21.
31. Erikson, A.; Tufto, I.; Bjonnum, A. B.; Bruland, O. S.; Davies, C. L. The Impact of Enzymatic Degradation on the Uptake of Differently Sized Therapeutic Molecules. *Anticancer Res.* **2008**, *28*, 3557–3566.